Proceedings of the ASME 2012 Fluids Engineering Summer Meeting
ASME FEDSM 2012
July 8-12, 2012, Rio Grande, Puerto Rico, USA

FEDSM2012-72354

CHARACTERISTICS OF PORESCALE VORTICAL STRUCTURES IN RANDOM AND ARRANGED PACKED BEDS OF SPHERES

Justin R. Finn *
Sourabh V. Apte
School of Mechanical Industrial
and Manufacturing Engineering
204 Rogers Hall
Oregon State University
Corvallis, Oregon 97331
Email: finnj@engr.oregonstate.edu
Email: sva@engr.oregonstate.edu

Brian D. Wood
School of Chemical Biological
and Environmental Engineering
103 Gleeson Hall
Oregon State University
Corvallis, Oregon 97331
Email: brian.wood@oregonstate.edu

ABSTRACT

The characteristics of pore scale vortical structures observed in moderate Reynolds number flow through monodisperse packed beds of spheres are examined. Our results come from direct numerical simulations of flow through (i) a periodic, simple cubic arrangement of 54 spheres, (ii) a wall bounded, close packed arrangement of 216 spheres, and (iii) a realistic randomly packed tube containing 326 spheres with a tube diameter to sphere diameter ratio of 5.96. Pore Reynolds numbers in the steady inertial ($10 \lesssim Re \lesssim 200$*) and unsteady inertial (*$Re \approx 600$*) regimes are considered. Even at similar Reynolds numbers, the vortical structures observed in flows through these three packings are remarkably different. The interior of the arranged packings are dominated by multi-lobed vortex ring structures which align with the principal axes of the packing. The random packing and the near wall region of the close packed arrangement are dominated by helical vortices, elongated in the mean flow direction. In the simple cubic packing, unsteady flow is marked by periodic vortex shedding which occurs at a single frequency. Conversely, at a similar Reynolds number, the vortical structures in unsteady flow through the random packing oscillate with many characteristic frequencies.*

*Address all correspondence to this author.

INTRODUCTION

The flow of fluid through a packed bed of spheres is a fundamental problem, rich in its applicability to a variety of disciplines. For example, groundwater hydrologists [1, 2], chemical engineers [3] and nuclear reactor designers [4] often consider flow through strikingly similar arrangements of fixed, contacting spheres as a prototypical problem for more complex systems. Despite such broad importance, the existing body of knowledge related to the flow physics of such problems is limited, particularly at moderate to large flow rates. For Stokesian, creeping flow, fluid streamlines conform naturally to the boundary of the porespace. In this case, the general behavior of the flow may be adequately described using geometric or network models [5], and simple relationships are available for macroscale properties such as *Darcy's law* for permeability. However, at larger flow rates, porous media and packed bed flows become highly non-linear and multiscale in nature due to the contribution of flow inertia. This makes a-priori determination of the flow characteristics difficult or impossible even for simple, homogeneous sphere packings.

This multiscale nature of inertial flows through porous media and packed beds is illustrated in FIG. 1. The *macroscale* is often used to describe the largest representative scale encountered in the field or laboratory. The macroscale flow can be sim-

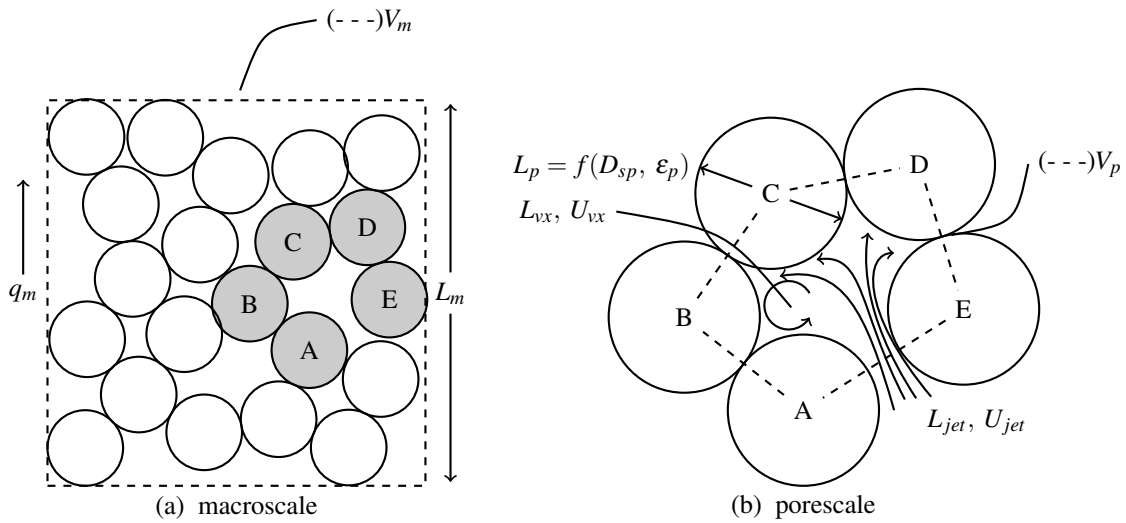

FIGURE 1: ILLUSTRATION OF THE MULTISCALE NATURE OF POROUS MEDIA FLOWS. (a) SHOWS A REPRESENTATIVE *MACROSCALE* VOLUME. (b) SHOWS THE *PORESCALE* WHERE COMPLEX HYDRODYNAMIC INTERACTIONS OCCUR.

ply characterized with a length scale L_m, volume V_m, porosity, ε_m and flux q_m. Typically it is macroscale properties including permeability, dispersion coefficients, or reaction rates which are of interest to practical engineering applications. Such properties derive from hydrodynamic interactions at the *porescale* or *Darcy scale*, shown as a single pore subset of the macroscale volume in FIG. 1b. At the porescale the length and volume scales are functions of the local pore geometry, $L_p,\ V_p = f(D_{sp},\ \varepsilon_p)$. These scales, along with the Reynolds number, govern the hydrodynamic character of the flow. We define the Reynolds number, following Ergun [6] and Dybbs & Edwards [7], as $Re = \frac{\rho U_p D_{sp}}{\mu} \cdot \frac{\varepsilon}{1-\varepsilon}$, where D_{sp} is the sphere diameter, $U_p = q_m/\varepsilon_m$ is the pore averaged flow velocity. As Reynolds number is increased from creeping flow rates, it has been observed both experimentally [7, 8], and computationally [9, 10] that the porespace becomes increasingly dominated by inertial flow features such as steady or unsteady jets, vortices, and stagnation regions.

Vortical flow features are of particular interest in porous media because of the implications they have for mixing and dispersion in the porespace. Vortices can enhance mixing by collecting streamlines from distant sources and ejecting them along new trajectories after exchange of fluid. Helical vortices with corkscrew trajectories are good examples of this, and are common features in inertial flows through porous media [10]. At unsteady Reynolds numbers, flow oscillations provide an effective means for enhancing fluid transport, and vortical features are often the backbone of these oscillations. Alternatively, vortices can act as *dead zones*, such as stationary recirculation bubbles in bluff body wakes, where entrained fluid is bounded by closed streamlines and residence time is high.

The case for detailed and accurate simulation to investigate these types of features is particularly compelling considering the challenges associated with making detailed three dimensional flow measurements in the interior of a solid sphere matrix, although new experimental techniques such as index of refraction matched PIV, and MRI are helping [11–14]. Broadly, resolved simulation methods used for flow through porous media can be classified by the way in which they represent the fluid/solid interface. To obtain a detailed description of the pore-scale flow field, appropriate boundary conditions (typically no-slip) need to be suitably enforced on the solid boundaries of the porespace, and the porespace needs to be sufficiently resolved by the computational grid. Body fitted grid methods, where the Navier Stokes equations are solved on unstructured grids that conform to the solid boundaries of the porespace, have probably been the most popular type of approach [15–18], and is the method which is pursued here. However, body fitted grid generation is complicated for porous media and packed bed geometries, and a care must be taken to avoid poor mesh quality, as described in the next section. Alternatives to the body fitted approach exist, including the *lattice-Boltzmann method*, *immersed boundary methods* and *fictitious domain methods*. The Lattice-Boltzmann method solves the Boltzmann equation of particle motion on a regular grid or *lattice*, which approximates the statistical distribution of fluid motion in space and time. This method has been used by Hill, Koch and coworkers [9, 10, 19, 20] to investigate inertial flows in packed beds and by Pilotti [21] in a synthetically generated porous medium. Immersed boundary and fictitious domain

methods, which have been applied widely to problems with complex or moving boundaries, are also beginning to see application to porous media flows [22, 23]. These methods use Cartesian, non body-conformal grids, and enforce surface boundary conditions with the addition of a local forcing term in the momentum equation. Recently Finn & Apte [23] have made comparisons of the traditional body fitted approach to a Cartesian grid fictitious-domain approach, and shown the latter to be favorable in terms of computational overhead required for accurate simulations of flow through packed beds.

The remainder of this paper will focus on the characterization of porescale vortical features in packed beds of spheres. These features are investigated using a parallel Navier-Stokes solver with unstructured, body fitted meshes. To understand the effects of the both flow inertia and solid geometry on these flow features, three different sphere packings are investigated at Reynolds numbers spanning the steady inertial ($10 \lesssim Re \lesssim 200$), and unsteady inertial flow $200 \lesssim Re \lesssim 1000$ regimes.

COMPUTATIONAL APPROACH

Consider the incompressible Navier-Stokes equations for the entire fluid domain:

$$\rho\left(\frac{\partial \mathbf{u}}{\partial t} + \mathbf{u}\cdot\nabla\mathbf{u}\right) = -\nabla p + \mu\nabla^2\mathbf{u} \quad (1)$$

$$\nabla\cdot\mathbf{u} = 0 \quad (2)$$

where ρ is the density, $\mathbf{u}$ the velocity vector, p the pressure, μ the fluid viscosity. The equations are discretized on unstructured, tetrahedral meshes, and solved using a parallel, second order accurate fractional step solver. The code is parallelized using Message Passing Interface (MPI), allowing for larger scale simulations by distributing the required memory over many processors. For additional details regarding the numerical implementation, the reader is referred to [24].

Unstructured mesh generation for complex geometries is a non-trivial procedure in general, and in packed beds the process is complicated by sphere-to-sphere contact points, near which elements can become unmanageably small and have high aspect ratios. We employ a cylinder bridge model [25], whereby every contact point is bridged by a small cylinder, removing a small amount of typically stagnant fluid as is illustrated in FIG. 2. This process has been parameterized and automated using the commercial package Pointwise®. Details regarding the mesh generation procedure as well as detailed validation of the flow solver for packed bed type problems can be found in [23].

FLOW THROUGH PACKED BEDS OF SPHERES

We now present results for flow through three different packed beds of spheres at both steady and unsteady Reynolds

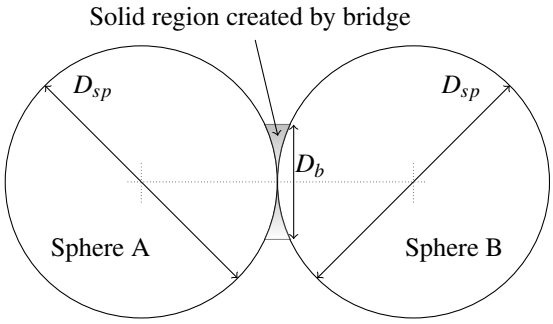

FIGURE 2: SCHEMATIC OF THE FILLET BRIDGE CREATED BETWEEN TWO CONTACTING SPHERES.

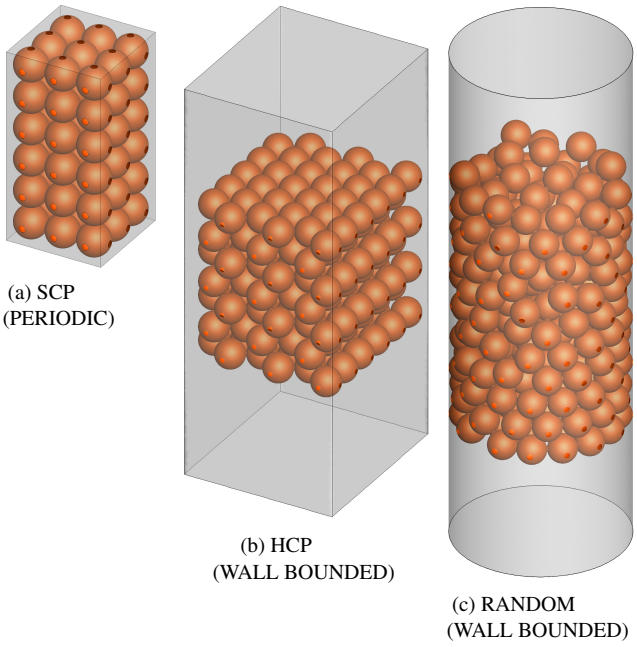

FIGURE 3: THE THREE SPHERE PACKINGS CONSIDERED. FLOW IS FROM BOTTOM TO TOP IN EACH CASE.

numbers. The sphere packings considered are shown in FIG. 3. Their characteristics, and the relevant parameters used in the simulations of flow through each are summarized in TAB. 1. The three packings were chosen to complement each other, as their porescale geometries vary significantly. The simple cubic packing (SCP) shown in FIG. 3a is the loosest possible packing arrangement with $\varepsilon_{SCP} = 0.47$. It contains periodic boundaries on all sides which allows for the generation of a flow field unaffected by the presence of external walls. Also, the repeating nature of the packing provides a single geometric length scale in the pore. A $3\times3\times3$ arrangement is used for the steady flows

TABLE 1: PACKED BED SIMULATIONS

	Packing	Dimension	Re	D_{sp}/Δ	N_{cv} total
Steady	SCP	$3\times3\times3$	$10<Re<250$	29	$1.2m$
	HCP	$6\times6\times6$	$10<Re<150$	29	$12.3m$
	Random	$D_{tube}/D_{sp}=5.96$, 326 sp. total	$10<Re<150$	29	$16.8m$
Unsteady	SCP	$3\times3\times6$	529	56	$7.3m$
	Random	$D_{tube}/D_{sp}=5.96$, 326 sp. total	600	56	$32m$

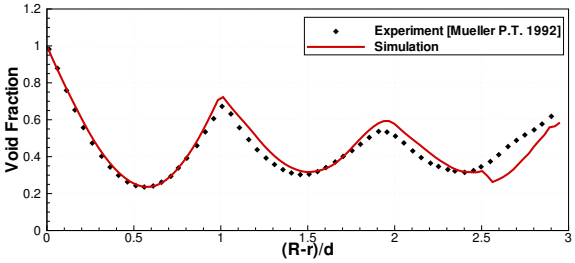

FIGURE 4: RADIAL VOID FRACTION VARIATION OF THE RANDOM PACKING. COMPARISON OF THE PRESENT SIMULATION TO THE EXPERIMENTALLY MEASURED VOID FRACTION OF MUELLER [27].

and a $3\times3\times6$ arrangement for the unsteady flows. The second packing is a $6\times6\times6$ hexagonal close packing containing (216 spheres) shown in FIG. 3b. It is one of two arrangements (face centered cubic being the other) with lowest possible void fraction of $\varepsilon=0.26$. However, this is only in the interior of the packing, and the solid, external boundaries result in a significantly higher mean void fraction, $\varepsilon_{HCP}=0.40$. This *wall effect* increases the Reynolds number near the wall and can lead to significant flow channeling. Finally, the packing shown in FIG. 3c is a tube packed randomly with 326 spheres. The tube diameter to sphere diameter ratio is $D_{tube}/D_{sp}=5.96$. The packing was generated following the parameterized, sequential procedure of Mueller [26] and has a mean void fraction of $\varepsilon_{random}=0.47$ and a total packing height of $h/D_{sp}\approx12$. Because of the exterior tube boundary, there is a significant wall effect in the radial porosity variation, $\varepsilon(r)$, which is shown in FIG. 4 alongside the void fraction variation of a laboratory generated packed column [27]. The trend of $\varepsilon(r)$ obtained with the current packing do a good job of matching the measured trend.

The pore volume of each geometry is meshed using the parameterized method described in [23]. All meshes used in the steady flow simulations have a grid spacing of $D_{sp}/\delta_{cv}\approx29$ which was shown to provide grid convergence and good experimental agreement in prototypical test cases. The unsteady simulations use a more refined mesh with $D_{sp}/\delta_{cv}\approx56$. The ratio of fillet diameter to sphere diameter is $D_f/D_{sp}=0.2$ for all simulations. The total number of tetrahedral control volumes, N_{cv} used in the body fitted meshes of each geometry varies from $1.2m$ to $16.8m$. The flow is forced in the positive Z direction by a constant pressure gradient in the SCP cases, and by a constant flux inflow condition in the HCP and random cases. Each simulation is started with the flow at rest, and the flow solution is advanced in a time accurate manner until the solution has reached a stationary state. In the steady flow cases, we use the total kinetic energy, $\sum_{cv}u_iu_i$, in the porespace as an indicator. When this quantity does not change significantly, the inflow flux or pressure gradient is increased to the next target Reynolds number. In the unsteady flow cases, the simulation is run for several non-dimensional flow through times, $\overline{T}=tU_p/D_{sp}$, so that the velocity fluctuations in the porespace reach a statistically stationary state.

STEADY FLOW

Steady Reynolds numbers were chose to thoroughly sample the inertial flow regime range between creeping flow ($Re\lesssim10$) and inertially dominated flow near the threshold of unsteadiness ($Re\gtrsim200$) [7]. The non-dimensional pressure drop, $\Psi=-\frac{\Delta P}{L_m}\frac{D_{sp}}{\rho U_p^2}\frac{\varepsilon_m}{1-\varepsilon_m}$ measures the relative resistance to flow through the packed bed. Here, ΔP is the difference in pressure measured at the outlet and inlet of the packing. This is plotted in FIG. 5 vs Reynolds number for each of the three packings. Also plotted are the correlations of Ergun [6] for infinite, random porous media, and Eisfeld & Schnitzlein's [28] correlation for randomly packed tubes with finite tube to sphere diameter ratios. The periodic SCP arrangement offers the least flow resistance at all Re, followed by the HCP arrangement. This is due in part to the preferential flow channeling between rows of spheres in the SCP arrangement and along the walls in the HCP arrangement. The random packing, which lacks long open channels, shows the highest resistance for all Re, and agrees reasonably well with the correlation from [28].

Next, the porescale vortical structures are examined in each arrangement. Due to the large amounts of shear in the porespace, using vorticity alone for vortex detection is generally noisy

and unfruitful. Instead, the λ_2 criteria of Jeong & Hussain [29] is used. This criteria identifies vortices as regions with a local pressure minima and can therefore be identified as regions where

$$\lambda_2(\mathbf{S}^2 + \Omega^2) < 0 \tag{3}$$

Here, $\mathbf{S}$ and Ω are the symmetric and anti-symmetric components of the velocity gradient tensor respectively, and the operator λ_2 returns the intermediate (second) eigenvalue of a symmetric matrix. In FIG.'s 6, 7 and 8, several visualizations are provided of the characteristic vortical structures seen in SCP, HCP, and random arrangements respectively. The SCP arrangement, shown in FIG. 6 is dominated by two distinct regions which can be identified easily with a simple streamline visualization (FIG. 6a): (i) high velocity channels through which the flow passes undisturbed, explaining the low values of Ψ, and (ii) large recirculation regions in the gaps between rows of spheres. These recirculation regions are actually complex, multi-lobed vortex ring structures, shown with an isosurface of λ_2 in FIG. 6b. These *vortex rings* are actually more like *vortex cubes*, with four distinct sides each aligned along a cross-stream axis. This is further illustrated in FIG. 6c, where the tangent vectors are plotted on a plane passing through the center of one of these vortex cubes, perpendicular to the mean flow. The vectors show the complex three-dimensionality of the flow feature, and the close relationship between the pore geometry and the behavior of the vortical structure.

The characteristic vortical structures observed in the HCP arrangement are shown in FIG. 7 as isosurfaces of λ_2. Similar to the SCP arrangement, the dominant porescale vortical feature in the interior of the packing is a multi-lobed vortex ring (FIG. 7a-b). These rings are located upstream of the forward stagnation points on the spheres in the interior of the packing. Due to the geometric orientation of the packing, the ring has 3 lobes which align with the principal axes of the packing as well as the major flow directions away from the stagnation point. Near the bounding walls, the flow is accelerated significantly due to the increased porosity and less tortuous channels compared to the interior. These factors give rise to elongated helical vortices shown in FIG. 7c. These helical structures are regions where the velocity and vorticity vectors are roughly aligned, and the flow spirals through the porespace with a roughly corkscrew motion.

This type of helical vortex is the dominant inertial feature everywhere in the random packing. In FIG. 8a-d, one typical feature is visualized using stream ribbons colored by λ_2, (red colors indicating the strongest vortical region) for $Re = 10,\ 50,\ 100,$ and 150, showing its development from near creeping flow to strongly inertial flow. The stream ribbons which enter the feature at all Re originate from two sides of the bottom sphere and collect in a channel where the streamwise flow is accelerated. As Re is increased from the creeping regime, flow inertia pushes

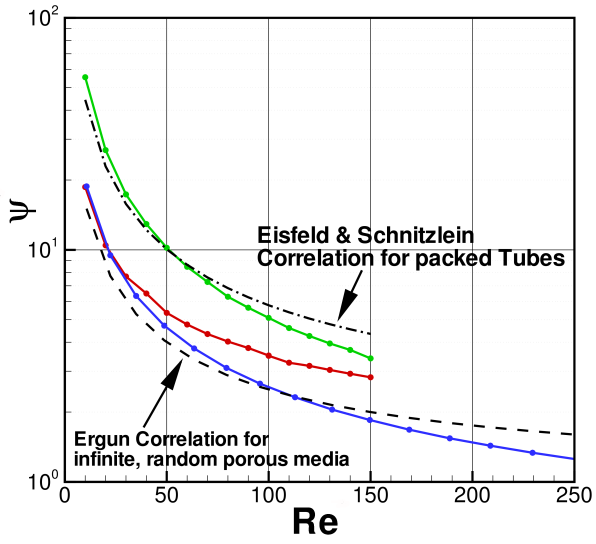

FIGURE 5: NON-DIMENSIONAL PRESSURE DROP AS A FUNCTION OF REYNOLDS NUMBER IN THE STEADY FLOW REGIME FOR THE THREE SPHERE PACKINGS. THE CORRELATIONS OF ERGUN [6] AND EISFELD & SCHNITZLEIN [28] ARE PLOTTED FOR COMPARISON.

the streamlines away from the right hand sphere, and the two streams entering the feature begin to twist around one another as they travel upward in a corkscrew like motion. This radial motion is non-existent at $Re = 10$ (FIG. 8a), first appears at $Re \approx 50$ (FIG. 8b), and strengthens with Re up to $Re = 150$ (FIG. 8c-d). Despite the variety of pores which exist in the random packing, this single feature is very representative of the majority of vortical structures seen for these steady flow rates. There are few, if any, of the vortex-ring like structures which were observed in the interior of the SCP and HCP arrangements, likely due to the lack of geometric symmetry and organization.

UNSTEADY FLOW

The random and SCP arrangements were chosen for unsteady flow simulations because of their distinctly different geometries and vortical structures observed in the steady flow regime. The simple cubic and random meshes used for these unsteady flows are composed of 7 million and 32 million CVs respectively. As in the steady flow cases, the mean flow is provided by a constant inflow condition on the bottom boundary in the random packing, and a constant pressure gradient in the triple periodic SCP arrangement. The resulting, time averaged Reynolds numbers are $Re = 600$ and $Re = 529$ respectively.

At $Re = 529$, the flow in the SCP arrangement is dominated by spatially and temporally periodic porescale vortex shedding. The characteristics of the three dimensional vortical structures

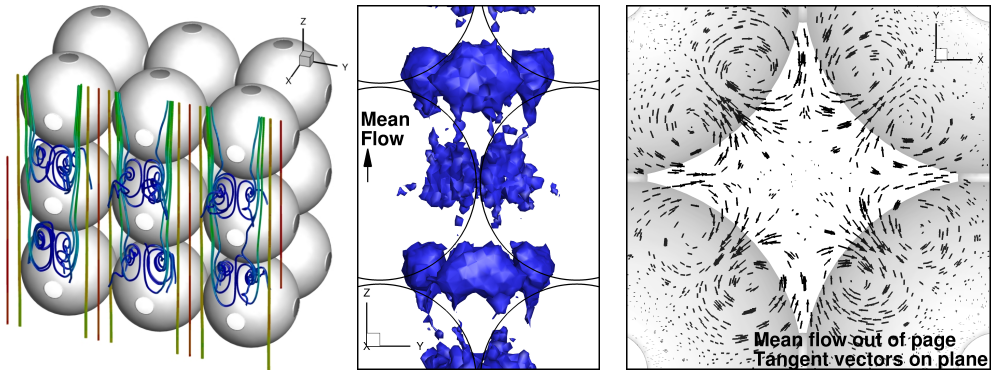

(a) (b) (c)

FIGURE 6: SCP FLOW AT $RE = 230$. (a) STREAMLINES COLORED BY STREAMWISE VELOCITY (RED = FAST), (b) ISO-SURFACES OF λ_2, (c) VELOCITY FIELD ON A CROSS-STREAM PLANE.

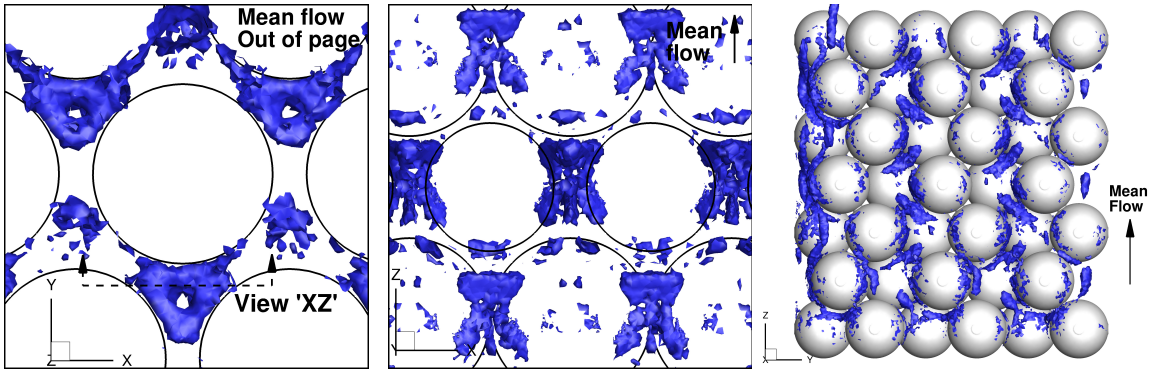

(a) (b) (c)

FIGURE 7: HCP FLOW AT $RE = 150$. ISOSURFACES OF λ_2 SHOWING THE INTERIOR VORTEX RING STRUCTURES (a,b), AND THE ELONGATED HELICAL VORTICES IN THE WALL REGION (c).

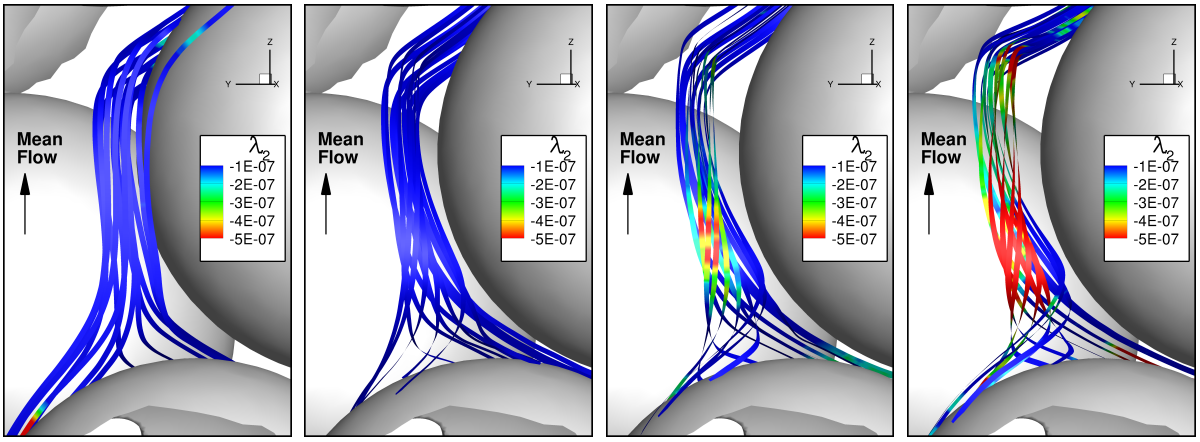

(a) $Re = 10$ (b) $Re = 50$ (c) $Re = 100$ (d) $Re = 150$

FIGURE 8: DEVELOPMENT OF A PORESCALE HELICAL VORTEX IN THE RANDOM ARRANGEMENT. STREAM RIBBONS COLORED BY λ_2 (RED INDICATES STRONG SWIRL).

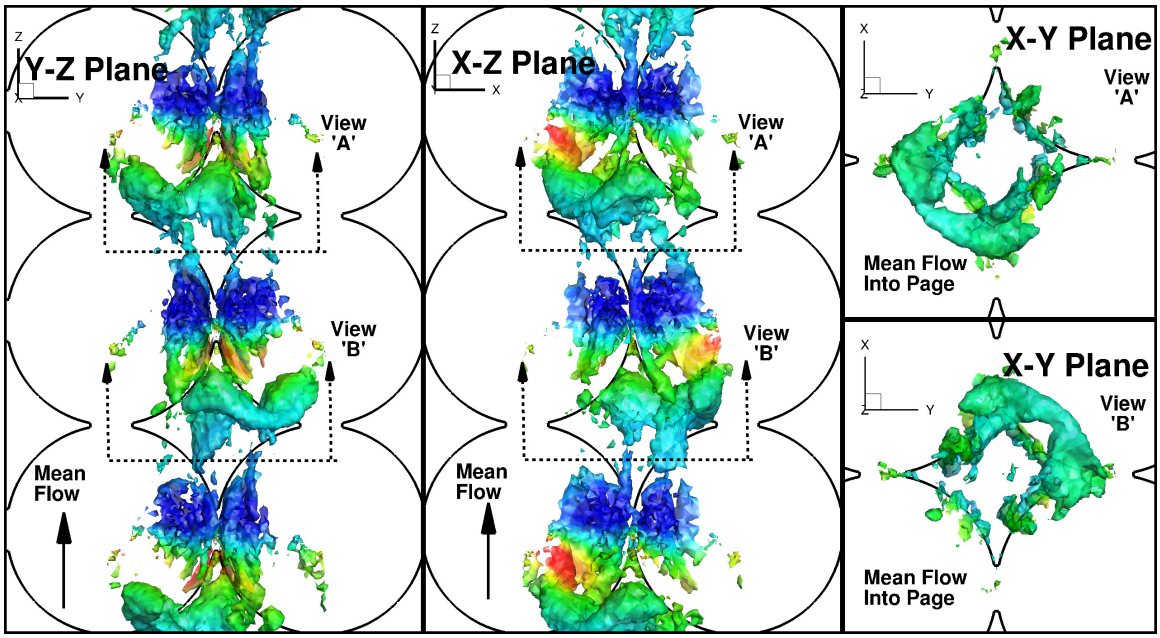

FIGURE 9: UNSTEADY PORESCALE KARMAN LIKE VORTEX SHEDDING OBSERVED IN THE SIMPLE CUBIC PACKING. ISOSURFACE OF λ_2 SHOWN, COLORED BY PRESSURE (BLUE INDICATES LOW PRESSURE REGION).

are shown in FIG. 9, where isosurfaces of λ_2 colored by local pressure are shown for a single snapshot in time. Several orthogonal views of consecutive pores, with sphere boundaries denoted with solid black lines, are provided to give three dimensional context to the vortical structure relative to the sphere packing. The main vortical feature in *every pore* is a half vortex ring which is bent upward in the direction of the mean flow. These half rings have a larger lobe at each end. These lobes are similar to the lobes observed in the steady flows through the SCP arrangement, in that they are aligned with the major cross-stream axes of the sphere packing (X and Y in this case). The difference however is that only two lobes exist at any given time in a single pore; the vortical structure never forms a complete, four lobed vortex ring as was seen for steady flow rates. These structures alternate spatially along the mean flow direction (Z), such that the half ring is located in opposite sides of consecutive pores. This is best seen in the X-Y views on the right hand side of FIG. 9. In the cross stream directions, these vortical features are *in phase* with one another. That is, across pores in the same X-Y plane, they will be located in the same quadrant of every pore (not shown).

The transient character of these structures strongly resembles the periodic Kármán vortex shedding observed in the wake of a single cylinder or sphere. The half vortex ring structures described above alternate between the $(+X,+Y)$ corner of the pore shown in View 'B' of FIG. 9 and the $(-X,-Y)$ corner shown in View 'A'. This 180^o phase shift occurs in every pore in the packing. In the middle of this cycle, the half ring structures are flushed into the high velocity channels by the mean flow, and are stretched into thinner tail-like regions. As a new half ring forms, the old structure is being flushed through the center of channel. These tail regions can be seen in the pore throats in the snapshot of FIG. 9.

Despite similar Reynolds numbers, the flow through the random packing contains remarkably different vortical structures. Due the the variety of geometric pore configurations which exist in this packing, the local value of Re can vary considerably from the bed average value of $Re = 600$. This results in not just one, but a variety of coherent porescale vortical structures. We will concentrate on the two main types of feature types seen, which are shown in FIG. 10. To illustrate these features, instantaneous stream-ribbons colored by the local pressure are shown in three different pores. The most common feature is the helical vortex, which was also seen at reduced flow rates in the steady flow simulations. In fact, the same pore is shown in FIG. 10a, as in FIG. 6g-k, and a helical vortex can be seen in a similar location as the one which develops over the range $50 < Re < 150$. At this higher, unsteady flow rate, the streamlines of the feature have much stronger radial motion as they spiral through the pore compared to the steady flow feature, and the length of the vortex is stretched further in the streamwise direction. These elongated helical vortices persist throughout the packing, often with multiple vortices in a single pore. Another of these features is shown in FIG. 10b, located near the solid outer tube wall. This feature results from the high momentum streamlines in the high void

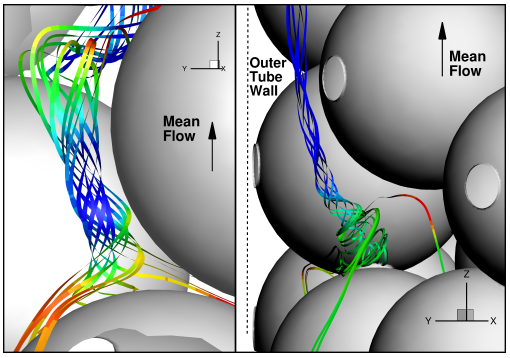

(a) (b)

INTERNAL AND EXTERNAL HELICAL VORTICES

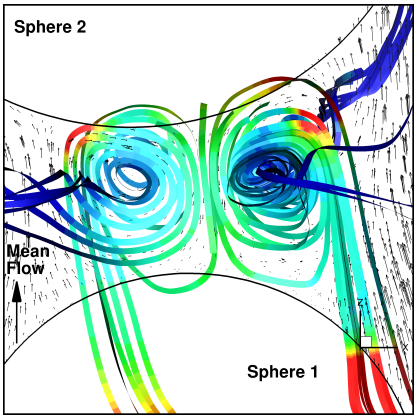

(c) COUNTER ROTATING VORTEX TUBES

FIGURE 10: UNSTEADY PORESCALE VORTICAL FEATURES OBSERVED IN THE RANDOM PACKING. STREAMRIBBONS COLORED BY PRESSURE ARE SHOWN IN THREE DIFFERENT PORES (BLUE INDICATES LOW PRESSURE REGION)

fraction wall region (see FIG. 4) mixing as they enter the pore from below, and swirling around each other during their exit upward. Because of the locally higher *Re* at the wall, and the other features that exist in this pore, this vortical feature is more *active* in it's unsteady motions than the internal feature of FIG. 10a, although it remains in this pore at all times. Future work will focus on quantifying the relationship between the vortical length and time scales and *Re* over the entire steady and unsteady flow regime.

The other main type of feature which is observed in the random packing at $Re = 529$ is a vortex tube whose axis is roughly aligned perpendicular to the flow. A counter-rotating pair of these features are shown in FIG. 10c. The instantaneous flow vectors in a perpendicular plane are shown in the background. Such features tend to exist in the near wake behind a sphere, or in the gaps between two spheres as shown. Despite the slow turnover time of these eddies exhibited by the vector magnitudes in the circulating regions, they are not complete dead zones. They expand and contract in tandem, meaning one grows while the other shrinks in a periodic fashion, exchanging fluid amongst themselves and with the mean flow.

None of the vortical features observed in the unsteady flow through the random packing exhibit any vortex shedding and there does not appear to be vortex destruction or creation at this Reynolds number. Rather, they tend to oscillate in their position without much net change of shape. The helical vortex cores translate periodically, mostly in the in the cross stream plane, but their size and mean location remains nearly constant for the length of the simulation.

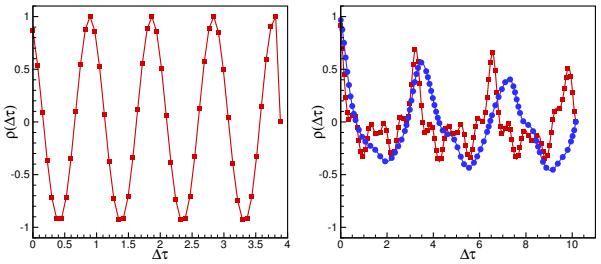

(a) SCP (b) Random

FIGURE 11: TIME AUTOCORRELATION FUNCTIONS OF STREAMWISE VELOCITY FLUCTUATIONS, ρ_{xx}. (–■–) SCP & RANDOM WALL REGION (OUTERMOST $0.5D_{sp}$), (●) RANDOM INNER CORE (INNERMOST $0.5D_{sp}$).

In order to quantify the timescales of these unsteady flows, the fluctuating velocity field, $\mathbf{u}'(x,t)$, is computed via a Reynolds decomposition for a time series of instantaneous velocity fields, $\mathbf{u}(\mathbf{x},t)$.

$$\mathbf{u}(\mathbf{x},t)' = \mathbf{u}(\mathbf{x},t) - \overline{\mathbf{u}}(\mathbf{x}) \tag{4}$$

Here, $\overline{\mathbf{u}}$ is the time averaged velocity field. With the fluctuating velocity field, the time autocorrelation function is computed for the porespace region of the SCP and random arrangements:

$$\rho_{ii}(\Delta\tau) = \sum_{\mathbf{x}}\sum_{\tau} \frac{u_i'(\mathbf{x},\tau)\, u_i'(\mathbf{x},\tau+\Delta\tau)}{u_i'(\mathbf{x},\tau)^2} \tag{5}$$

$$\tag{6}$$

Here, $\Delta\tau = \frac{tU}{D_{sp}}$ is the non-dimensional time separation, between two velocity samples at position $\mathbf{x}$ in the porespace. The streamwise autocorrelation function, ρ_{xx} is plotted for both arrangements in FIG. 11. The cross-stream correlation functions, ρ_{yy} and

ρ_{zz}, show similar trends in both arrangements and are omitted for clarity. The SCP time correlation function is periodic with a single dominant frequency. Recently, Horton & Pokrajac [14] have experimentally investigated the flow structure in SCP arrangements of spheres driven by constant pressure gradients with ultrasonic velocity profilers (UVP), and observed similar periodic correlation functions at transitional Reynolds numbers. These resolved simulation results, which show the shedding and motion of coherent vortical structures at the porescale, provide corroborating evidence that these periodic velocity fluctuations are linked to porescale vortical motion and vortex shedding .

Because of the radial porosity variations present in the random packing (FIG. 4), and the locally higher *Re* near the wall, the correlation function is computed *separately* for different annular regions of the flow to show the effect of the wall on the unsteady timescales. In FIG. 11b we have plotted the function for the region within $0.5D_{sp}$ of the tube wall and the region within $0.5D_{sp}$ of the tube centerline. These two correlations both show time periodic behavior, and the existence of several modes of velocity fluctuations in the porespace. The higher Reynolds number wall region shows exhibits a more complex function with more modes than does the inner region. Both correlation functions decay with long time separation, similar to the results of [30] for converging/diverging channel flows, but shows a strongly periodic behavior for the short time separations investigated here. This shows that despite the randomness of the bed, there are very specific dominant modes of velocity fluctuation. The increased number of modes compared to the SCP arrangement signals that the flow through the random packing may be closer to a turbulent chaotic breakdown.

By performing a Fourier transform on the autocorrelation functions, the velocity frequency spectra can be obtained. This is shown in FIG. 12 for both sphere arrangements, where the frequency is non-dimensionality to give the Strouhal number, $St = (\Delta\tau)^{-1}$. The SCP arrangement contains a dominant Strouhal number of nearly unity, showing the vortex shedding is strongly linked to the length scale of the sphere packing. The random packing contains several different Strouhal numbers between 0.29 and 1.57. In the inner region, the high frequency modes ($St > 1$ have been eliminated. This shows that the larger Reynolds number wall region contains a larger spectrum of energetic time (and most likely spatial) scales,

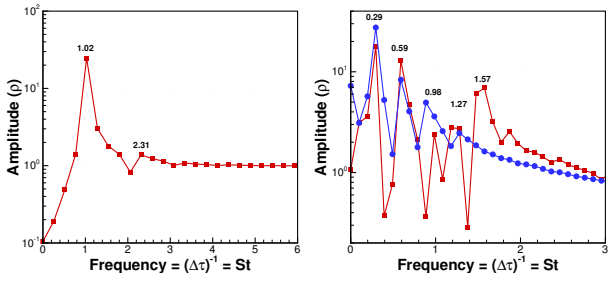

(a) SCP (b) Random

FIGURE 12: VELOCITY FREQUENCY SPECTRUM OBTAINED FROM THE FOURIER TRANSFORM OF ρ_{xx}. (–■–) SCP & RANDOM WALL REGION (INNERMOST $0.5D_{sp}$), (●) RANDOM INNER CORE (INNERMOST $0.5D_{sp}$)

CONCLUSIONS

Resolved and time accurate simulations of flows through three different types of packed bed geometries have been performed to identify and characterize pore scale vortical structures. These simulations considered the steady and unsteady inertial regimes ($10 < 600$), where the effect of porescale flow features on macroscale properties is not well understood. Vortical features are detected by regions of swirl and pressure minima using the λ_2 criteria. The results show that there is a clear relationship between pore geometry and the types of pore-scale vortical structures observed. In the SCP and HCP arrangements, a multilobed vortex ring structure is present in the gaps between spheres at steady flow rates. The lobes of these structures align with the principal geometric axes of the packing, and are highly three dimensional. At steady flow rates through the random packing, and in the wall region of the HCP arrangement, elongated helical vortices are the dominant porescale flow feature. Such features appear to be located near accelerating streamlines in regions of high curvature and low geometric symmetry.

At higher flow rates near $Re = 600$, the unsteady dynamics of flow through the SCP and random arrangements are significantly different. In the simple cubic arrangement, spatially and temporally periodic Kármán like vortex shedding is observed at a single Strouhal number near 1. Flow through the random arrangement exhibits a wider range of time scales with Strouhal numbers between 0.29 and 1.57 but without any observed vortex shedding. The higher frequency modes seem to be active mostly in the near wall region, where the Reynolds number is locally higher due to the wall effect. At this Reynolds number, helical vortices are still the dominant porescale feature, along with vortex tubes aligned perpendicular to the mean flow.

Future work on this topic will focus on quantifying the length and time scales of the porescale vortical features identified here, and linking their characteristics to macroscale properties. Also, direct comparison with experimental measurements in similar packed beds will be used as more detailed validation of the computational methods.

ACKNOWLEDGMENT

This work was supported by the National Science Foundation (Project #0933857: *Inertial Effects in Flow Through Porous Media*). Simulations were performed using resources provided

by the Texas Advanced Computing Center.

REFERENCES

[1] Wood, B., 2007. "Inertial effects in dispersion in porous media". *Water Resources Research,* ***43***(12), p. 12.

[2] Rashidi, M., Peurrung, L., Tompson, A., and Kulp, T., 1996. "Experimental analysis of pore-scale flow and transport in porous media". *Advances in Water Resources,* ***19***(3), pp. 163–180.

[3] Dixon, A., and Nijemeisland, M., 2001. "CFD as a design tool for fixed-bed reactors". *Ind. eng. chem. res,* ***40***(23), pp. 5246–5254.

[4] Hassan, Y., 2008. "Large eddy simulation in pebble bed gas cooled core reactors". *Nuclear Engineering and Design,* ***238***(3), pp. 530–537.

[5] Blunt, M., 2001. "Flow in porous media–pore-network models and multiphase flow". *Current opinion in colloid & interface science,* ***6***(3), pp. 197–207.

[6] Ergun, S., 1952. "Fluid flow through packed columns". *Chem. Eng. Prog,* ***48***(2), pp. 89–94.

[7] Dybbs, A., and Edwards, R., 1984. "A new look at porous media fluid mechanics–Darcy to turbulent". *Fundamentals of transport phenomena in porous media*, pp. 199–254.

[8] Suekane, T., Yokouchi, Y., and Hirai, S., 2003. "Inertial flow structures in a simple-packed bed of spheres". *AIChE Journal,* ***49***(1), pp. 10–17.

[9] Hill, R., Koch, D., and Ladd, A., 2001. "Moderate-Reynolds-number flows in ordered and random arrays of spheres". *Journal of Fluid Mechanics,* ***448***, pp. 243–278.

[10] Hill, R., and Koch, D., 2002. "The transition from steady to weakly turbulent flow in a close-packed ordered array of spheres". *Journal of Fluid Mechanics,* ***465***, pp. 59–97.

[11] Arthur, J., Ruth, D., and Tachie, M., 2009. "Piv measurements of flow through a model porous medium with varying boundary conditions". *Journal of Fluid Mechanics,* ***629***(1), pp. 343–374.

[12] Huang, A. Y. L., Huang, M. Y. F., Capert, H., and Chen, R.-H., 2008. "Optical measurements of pore geometry and fluid velocity in a bed of irregularly packed spheres". *Experiments in Fluids,* ***45***, pp. 309–321.

[13] Stohr, M., Roth, K., and Jahne, B., 2003. "Measurement of 3D pore-scale flow in index-matched porous media". *Experiments in Fluids,* ***35***(2), pp. 159–166.

[14] Horton, N., and Pokrajac, D., 2009. "Onset of turbulence in a regular porous medium: An experimental study". *Physics of fluids,* ***21***, p. 045104.

[15] Dixon, A., Nijemeisland, M., and Stitt, E., 2006. "Packed tubular reactor modeling and catalyst design using computational fluid dynamics". *Computational Fluid Dynamics*, p. 307.

[16] Atmakidis, T., and Kenig, E., 2009. "CFD-based analysis of the wall effect on the pressure drop in packed beds with moderate tube/particle diameter ratios in the laminar flow regime". *Chemical Engineering Journal*.

[17] Guardo, A., Coussirat, M., Recasens, F., Larrayoz, M., and Escaler, X., 2006. "CFD study on particle-to-fluid heat transfer in fixed bed reactors: Convective heat transfer at low and high pressure". *Chemical Engineering Science,* ***61***(13), pp. 4341–4353.

[18] Nelson, B., 2009. "Scaling analysis for the pebble bed of the very high temperature gas-cooled reactor thermal hydraulic test facility". PhD thesis, Oregon State University.

[19] Hill, R., Koch, D., and Ladd, A., 2001. "The first effects of fluid inertia on flows in ordered and random arrays of spheres". *Journal of Fluid Mechanics,* ***448***, pp. 213–241.

[20] Hill, R., and Koch, D., 2002. "Moderate-Reynolds-number flow in a wall-bounded porous medium". *Journal of Fluid Mechanics,* ***453***, pp. 315–344.

[21] Pilotti, M., 2003. "Viscous flow in three-dimensional reconstructed porous media". *International Journal for Numerical and Analytical Methods in Geomechanics,* ***27***(8), pp. 633–649.

[22] Ovaysi, S., and Piri, M., 2010. "Direct pore-level modeling of incompressible fluid flow in porous media". *Journal of Computational Physics,* ***229***(19), pp. 7456–7476.

[23] Finn, J., and Apte, S., 2012. "Relative performance of body-fitted and fictitious-domain simulations of flow through porous media". *ASME Fluids Engineering Summer Meeting,* ***Submitted for publication***(FEDSM2012-72355).

[24] Moin, P., and Apte, S., 2006. "Large-Eddy Simulation of Realistic Gas Turbine-Combustors". *AIAA Journal,* ***44***(4), pp. 698–708.

[25] Kuroki, M., Ookawara, S., and Ogawa, K., 2009. "A High-Fidelity CFD Model of Methane Steam Reforming in a Packed Bed Reactor". *Journal of Chemical Engineering of Japan,* ***42***(Supplement.), pp. 73–78.

[26] Mueller, G., 2005. "Numerically packing spheres in cylinders". *Powder technology,* ***159***(2), pp. 105–110.

[27] Mueller, G., 1992. "Radial void fraction distributions in randomly packed fixed beds of uniformly sized spheres in cylindrical containers". *Powder technology,* ***72***(3), pp. 269–275.

[28] Eisfeld, B., and Schnitzlein, K., 2001. "The influence of confining walls on the pressure drop in packed beds". *Chemical Engineering Science,* ***56***(14), pp. 4321–4329.

[29] Jeong, J., and Hussain, F., 1995. "On the identification of a vortex". *Journal of Fluid Mechanics,* ***285***(1), pp. 69–94.

[30] Guzman, A., and Amon, C., 1996. "Dynamical flow characterization of transitional and chaotic regimes in converging–diverging channels". *Journal of Fluid Mechanics,* ***321***(1), pp. 25–57.